Weyl node assisted conductivity switch in interfacial phase-change memory with van der Waals interfaces

Jinwoong Kim,[1,*] Jeongwoo Kim,[2] Young-Sun Song,[3] Ruqian Wu,[2] Seung-Hoon Jhi,[3] and Nicholas Kioussis[1,†]
[1]*Department of Physics and Astronomy, California State University, Northridge, California, USA*
[2]*Department of Physics, University of California, Irvine, California, USA*
[3]*Department of Physics, Pohang University of Science and Technology, Pohang, Korea*
(Received 2 July 2017; published 11 December 2017)

The interfacial phase-change memory (iPCM) $GeTe/Sb_2Te_3$, a promising candidate for the next generation nonvolatile random-access memories, exhibits fascinating topological properties. Depending on the atomic-layer-stacking sequence of the GeTe block, the iPCM can be either in the SET (Ge-Te-Ge-Te) or RESET (Te-Ge-Ge-Te) states, where the former exhibits ferroelectric polarization and electrical conductivity two orders of magnitude larger than that of the RESET state. Yet, its microscopic origin remains elusive. Here, we predict the emergence of a Weyl semimetal phase in the SET state induced by the ferroelectric polarization which breaks the crystal inversion symmetry. We show that the giant conductivity enhancement of the SET phase is due to the appearance of gapless Weyl nodes. The Ge-Te- or Sb-Te-terminated surfaces of Weyl semimetal iPCM exhibit surface states with completely distinctive topology, where the former consists solely of Fermi arcs while the latter consists of both closed Fermi surface and open Fermi arcs. The iPCM with van der Waals interfaces offers an ideal platform for exploiting the exotic Weyl properties as well as for future memory device applications.

DOI: 10.1103/PhysRevB.96.235304

Among the chalcogenide phase-change materials, the $Ge_2Sb_2Te_5$ (GST) compound, which undergoes a reversible structural transition between the crystalline and amorphous phases, continues to be the subject of intense interest because of its high potential for nonvolatile phase-change memory (PCM) devices [1–5]. However, a bottleneck is the high energy consumption during the transition process to the amorphous phase. A major breakthrough was the discovery of an *interfacial* phase-change memory (iPCM) [6], which retains the crystalline structure in both the high- (SET) and low-conductivity (RESET) states. It offers reduction in switching energies more than 95% compared to the conventional PCM as well as improved write-erase cycle lifetimes and faster switching speeds.

The structures in the two memory states of the iPCM are revealed to consist of a two-component $(GeTe)_n/(Sb_2Te_3)_m$ superlattice. The switch process involves a one-dimensional atomic motion normal to the interface. More explicitly, the stacking sequences within the GeTe layers in the SET and RESET phases are . . .-Te-Ge-Te-Ge-. . . and . . .-Te-Ge-Ge-Te-. . ., respectively. While the former exhibits ferroelectric polarization due to the breaking of the crystal inversion symmetry [6,7], the latter has no polarization. The underlying mechanism of the phase-change dynamics has been intensively studied [8]. However, the effect of the local structural transition on the giant change of resistance (up to two orders of magnitude) [9] has not been addressed yet.

A cornerstone of modern condensed-matter physics is the discovery of topolgical states of matter that may accelerate the development in spintronics and open a way to realize massless particle equations such as Dirac and Weyl fermions [10–17]. A Weyl semimetal (WSM) is a topological semimetallic material hosting gapless nodes near the Fermi level in the three-dimensional (3D) momentum space where the nodes correspond to effective magnetic monopoles or antimonopoles [13–17]. One important feature of the WSM is surface states which form open Fermi arcs rather than closed loops [16,17]. Compared to their Dirac semimetal counterparts, WSM requires the breakdown either of time reversal or inversion symmetry to split each degenerate Dirac node into a pair of Weyl nodes.

One important property of the RESET state of the iPCM is the time-reversal nontrivial topological order inherited from the bulk Sb_2Te_3 [18,19], although the band inversion strength is somewhat reduced by the intercalating GeTe block [20,21]. In the SET state, the GeTe block not only reduces the band inversion strength but also breaks the spatial inversion symmetry due to its inherent ferroelectric polarization [22,23]. Consequently, the superlattice consisting of alternating topological insulator (TI) and ferroelectric insulator thin films may offer a simple realization of a WSM phase [24,25], in analogy to the magnetically doped 3D topological insulator-trivial insulator superlattice [26].

In this report, employing *ab initio* electronic structure calculations we predict that the SET phase of the iPCM is an ideal WSM with (1) Weyl nodes lying on the Fermi level without intervening bulk states and (2) van der Waals bonding layers. We also elucidate that the underlying mechanism of the giant enhancement (by up to two orders of magnitude) of the electrical conductivity as the iPCM undergoes the phase transition from the RESET to the SET state is the emergence of the gapless Weyl nodes.

The density functional theory calculations were carried out using the Vienna *ab initio* simulation package (VASP) [27,28]. The pseudopotential and wave functions are treated within the projector-augmented wave (PAW) method [29,30]. Structural relaxations were carried out using the generalized gradient approximation as parameterized by Perdew *et al.* [31] with van der Waals corrections [32]. The plane-wave cutoff energy is

*jinwoong.kim@csun.edu
†nick.kioussis@csun.edu

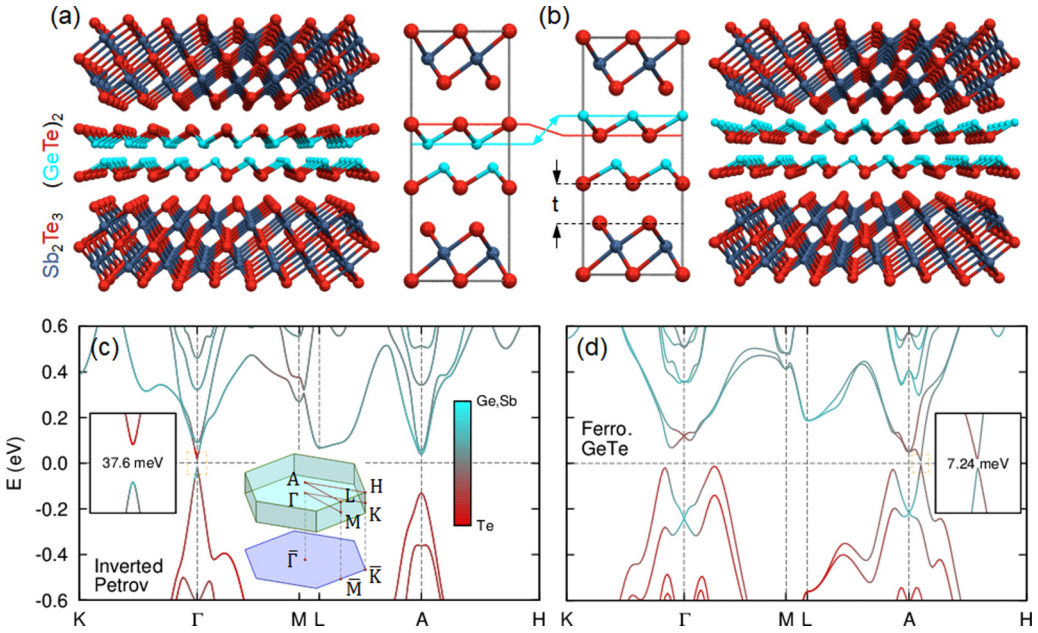

FIG. 1. Atomic and electronic structures of iPCM in the RESET and SET states. Side view of the hexagonal $(GeTe)_2(Sb_2Te_3)_1$ superlattice in the (a) RESET inverted-Petrov structure (Sb_2Te_3-Te-Ge-Ge-Te- stacking) and (b) SET ferroelectic-GeTe structure (Sb_2Te_3-Ge-Te-Ge-Te- stacking). MBJLDA bulk band structure along symmetry lines of (c) inverted-Petrov and (d) ferro-GeTe band structures with the Fermi level set at 0 eV. The bands denoted with red (cyan) derive from anion (cation) states. Inset shows the bulk BZ with the high symmetry points and the projected 2D BZ for the (001) surface.

400 eV and a $15 \times 15 \times 5\,k$ point mesh is used in the Brillouin zone (BZ) sampling. The electronic properties such as the band structures, surface states, and conductivities have been calculated using the tight-binding parameters obtained from vasp-wannier90 calculations [33]. In the Wannier function projection, the modified Becke-Johnson local density approximation (MBJLDA) [34,35] potential was employed, which has been shown to yield accurate band gaps, effective masses, and frontier-band ordering. Spin-orbit coupling was included in the projection with a $10 \times 10 \times 4\,k$-point mesh in the BZ sampling. The Weyl nodes were traced using a steepest decent method while the longitudinal electric conductivity was calculated within the semiclassical Boltzmann transport theory [33].

Figures 1(a) and 1(b) show the crystal structure of the $(GeTe)_2(Sb_2Te_3)_1$ superlattice in the highly resistive RESET state with Sb_2Te_3-Te-Ge-Ge-Te- stacking sequence (inverted-Petrov structure) and the highly conductive SET state with Sb_2Te_3-Ge-Te-Ge-Te- stacking sequence (ferroelectic-GeTe structure) along the rhombohedral [111] direction. The calculated equilibrium structural parameters for both the RESET and SET phase are listed in Table I. The calculated values of the c lattice parameters are in good agreement with the experimental values of 18.6 Å and 17.6 Å for the RESET and SET phases, respectively [7]. The Sb_2Te_3 block consists of one Te-Sb-Te-Sb-Te quintuplet layer. Despite the large contrast in electrical conductivity, the sole difference in atomic structure is the stacking sequence of Ge-Te layers sandwiched by Sb_2Te_3 layers.

TABLE I. Calculated equilibrium lattice constants, thickness of the building blocks, d, and the Te-Te spacing in Å.

Phase	a	c	$d(Ge_2Te_2)$	$d(Sb_2Te_3)$	t(Te-Te)
RESET	4.139	18.309	4.646	7.562	3.050
SET	4.203	17.385	4.968	7.499	2.893

The MBJLDA band structures along the high-symmetry directions for the (a) inverted-Petrov and (b) ferro-GeTe $(GeTe)_2(Sb_2Te_3)_1$ superlattices are shown in Figs. 1(c) and 1(d), respectively. As expected, the RESET state shows an inverted band structure at Γ where the conduction band minimum is derived primarily from Te-p states while the valence band maximum from cation (Ge or Sb) p states, indicating that the RESET state is a TI, in agreement with a previous study [20]. The direct energy gap of 38 meV at the Γ point which is smaller by a factor of 5 than that of Sb_2Te_3 [36] indicates a reduction in the band inversion strength and thus proximity of the system to the boundary between topological and normal insulator (NI) phases. Despite the conducting nature of the surface states protected by the nontrivial band topology, the electric conduction is mostly dominated by the insulating bulk states, rendering the RESET state highly resistive. On the other hand, the emergence of ferroelectric polarization in the SET state induces a giant Rashba effect that lifts the degeneracy around Γ and A. As a result, the valence band maxima and conduction band minima shift away from these symmetry points. Despite these differences, both RESET and SET states show gapped band structures along the high symmetry directions and hence may not explain the striking conductivity change across the phase transition. Obviously, it is natural to examine if the SET state is a WSM by searching the Weyl nodes in the entire BZ.

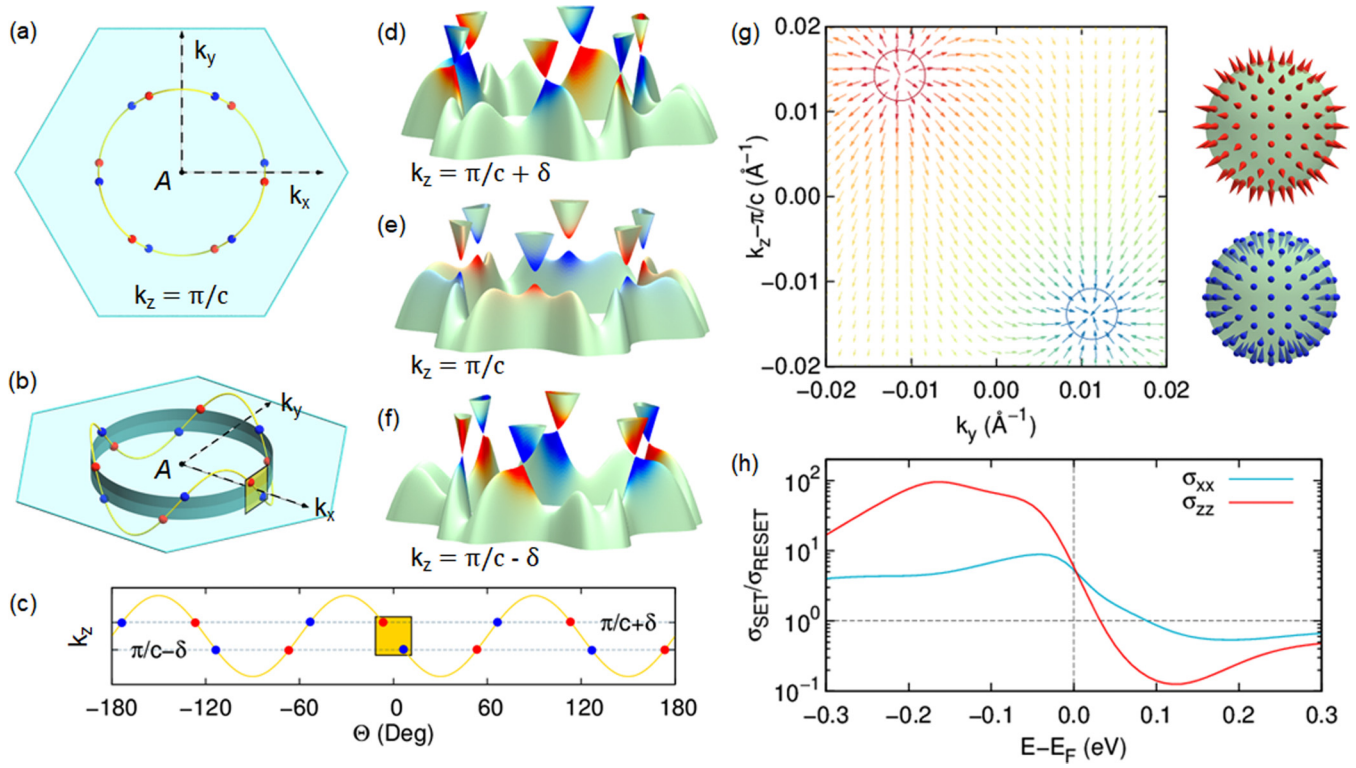

FIG. 2. Weyl nodes and conductivity enhancement in the SET state. (a) Top view and (b) oblique view of locations of Weyl nodes in the BZ of the ferro-GeTe structure, where red (blue) circles denote Weyl nodes with positive (negative) chirality. The hexagon denotes a cross section of BZ at $k_z = \pi/c$. The position of Weyl nodes relative to A point is scaled fivefold bigger for visibility. (c) Location of Weyl nodes along the k_z direction vs the azimuthal angle θ in the k_x-k_y plane. The yellow curve is a fitted sinusoidal curve for a guide. [(d)–(f)] Calculated bulk band structures of ferro-GeTe structure on the 2D k_x-k_y plane at (d) $k_z = \pi/c + \delta$, (e) π/c, and (f) $\pi/c - \delta$, respectively, where $\delta = 0.0143$ Å^{-1} is the deviation of Weyl nodes from the BZ cross section. Red and blue colors in panel (e) denote the $\hat{z}$ component of Berry curvature, Ω_z, while those in panels (d) and (f) denote the chirality, $\sum_i \Delta\mathbf{k}_i \cdot \Omega(\mathbf{k})/(|\Delta\mathbf{k}_i|\exp(|\Delta\mathbf{k}_i|/r_0))$. Here $\Delta\mathbf{k}_i = \mathbf{k} - \mathbf{k}_i$, where $\mathbf{k}_i$ is each Weyl node position and r_0 is an arbitrary cutoff radius. (g) Distribution of Berry curvature on a part of the k_y-k_z plane [yellow highlighted square in panel (b)]. (h) Calculated in- and out-of-plane conductivity ratio of the SET to RESET states as a function of the chemical potential.

Interestingly, we find that the SET state is indeed a WSM with twelve gapless Weyl nodes at the Fermi level in the vicinity of the A point. Figures 2(a), 2(b) and 2(c) show three pairs of Weyl nodes located at the $k_z = \pi/c + \delta$ plane and the other three pairs at the $\pi/c - \delta$ plane, respectively, where $\delta = 0.0143$ Å^{-1} is the deviation from the BZ cross section at $k_z = \pi/c$. The distances between the nearest and next-nearest Weyl nodes are 0.036 Å^{-1} and 0.079 Å^{-1}, respectively. The two-dimensional band structure of the SET state in the $k_x - k_y$ planes at $k_z = \pi/c + \delta$, $k_z = \pi/c$, and $k_z = \pi/c - \delta$ are shown in Figs. 2(d), 2(e) and 2(f), respectively. One can clearly see that the SET state is gapped at the BZ boundary $k_z = \pi/c$, while it is gapless, having six Weyl nodes each at two planes away from the BZ boundary. The calculated Berry curvature shows more detailed characteristics of the Weyl phase in the SET state. Each Weyl node behaves as an effective magnetic monopole in the momentum space with either positive or negative chirality, corresponding to a source or a sink of the Berry curvature, respectively. In Fig. 2(g), we show the Berry curvature with a dense k-point grid on the $k_y - k_z$ plane that passes through the two Weyl nodes, clearly indicating the outgoing and incoming flux of Berry curvature from one monopole (red) to the other monopole (blue).

Unlike Dirac nodes, which may easily become massive by weak perturbations, Weyl nodes are persistently massless until they are mutually annihilated. Furthermore, the chirality of Weyl nodes prohibits the back scattering of conduction electrons from each chiral channel. The emergence of gapless nodes characterized by an exceptional high mobility, therefore, may explain the giant conductivity enhancement as iPCM undergoes the RESET to SET phase transition. By employing the maximally localized Wannier functions and the semiclassical Boltzmann transport equation in the constant relaxation time approximation, we calculated the room-temperature electric conductivity of the SET and RESET states, under the assumption that both states have the same relaxation time. Figure 2(h) shows the ratio of the SET to the RESET state of both the in- and out-of-plane conductivity as a function of the chemical potential. Our calculations show that for both transport directions, $\sigma_{\mathrm{SET}} \sim 5.6\sigma_{\mathrm{RESET}}$ at $E = E_F$. On the other hand, the conductivity ratio may increase by up to two orders of magnitude for p-doped cases, which commonly occur in PCM due to Ge vacancies. Therefore, we can attribute the giant change of conductivity observed in experiment [9] to the presence of Weyl nodes. This is an important connection between Weyl state and the transport property of a real material.

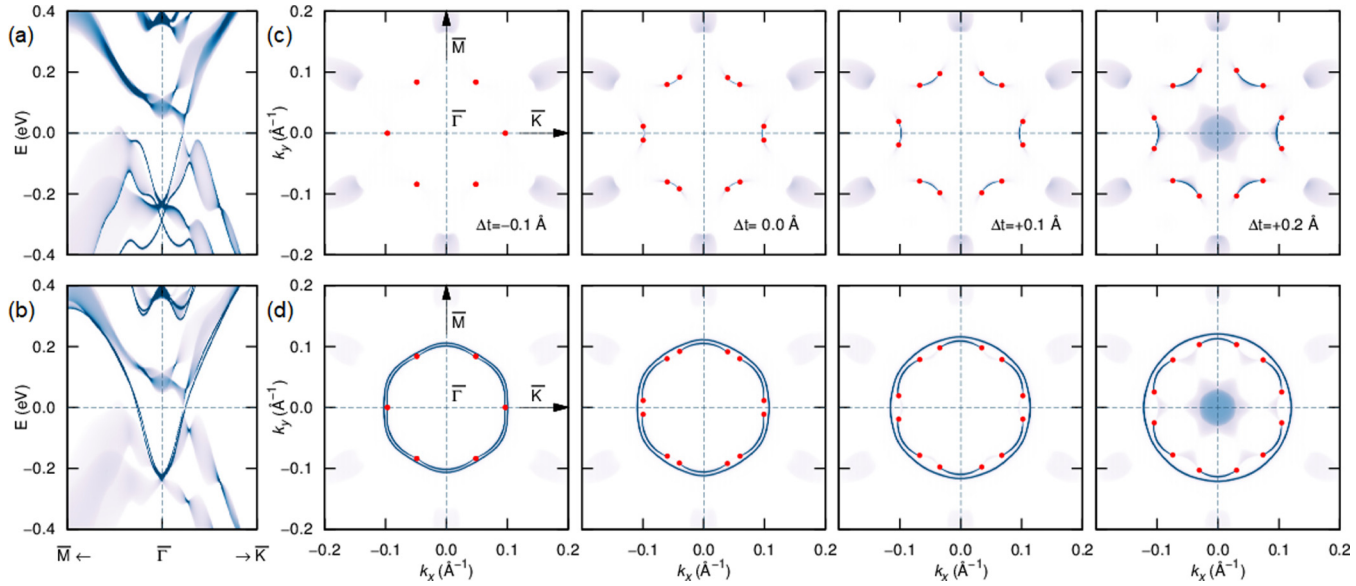

FIG. 3. (001) surface states of the semi-infinite iPCM structure in the SET state. Surface band structures for (a) GTT surface and (b) STT surface. Fermi surfaces on (c) the GTT and (d) the STT surfaces as a function of the change of vacancy layer thickness from its equilibrium value, $\Delta t = t - t_{eq}$, where t is shown in Fig. 1(b). Red dots denote Weyl nodes projected on the surface BZ.

For the experimental verification of the Weyl state, we next address another key characteristic of a WSM: the presence of the Fermi arc surface states that connect the Weyl nodes in pairs on the surface BZ. Using the Green's function method based on the tight-binding Hamiltonian generated by the Wannier projection scheme, we obtain the surface band structures of the Ge-Te-terminated (GTT) and the Sb-Te-terminated (STT) surfaces. The band structure of the GTT surface [Fig. 3(a)] illustrates typical features of the Weyl phase, namely it is gapped along the $\bar{\Gamma}$-$\bar{M}$ direction while it is gapless along the $\bar{\Gamma}$-$\bar{K}$ direction. This is consistent with the Fermi arcs in the second panel of Fig. 3(c) connecting Weyl pairs across the $\bar{\Gamma}$-$\bar{K}$ axis. On the other hand, the band structure on the STT surface [Fig. 3(b)] is not trivial as the GTT surface. The STT surface bands cross the Fermi level along both the high symmetry lines indicating a closed loop on the surface [the second panel of Fig. 3(d)]. Interestingly, the STT surface indeed displays one closed loop together with six Fermi arcs which rather connect counter-Weyl-node pairs compared to the GTT surface. The relation between the Fermi-arc-connected pairs and the emergent closed loop is elucidated below.

Because of shorter out-of-plane lattice constant (17.385 Å) of the SET state compared to that (18.309 Å) of the RESET state, the domain in the SET state may experience tensile uniaxial strain from surrounding domains in the RESET state. Assuming that the van der Waals bonding is mostly affected by the external strain, we have determined the evolution of the surface state with varying vacancy layer thickness, t, defined in Fig. 1(b). Our calculations reveal that under compressive strain the six pairs of Weyl nodes merge along the $\bar{\Gamma}$-$\bar{K}$ direction and disappear, while the WSM phase remains intact under tensile strain. Therefore, the WSM phase in the SET state would persist even under potential environmental tensile strain.

The distinct behavior of the Fermi arcs on the GTT and STT surfaces of the SET state can be understood as two different adiabatic transition pathways (shown schematically in Fig. 4) of surface states from the normal to the topological insulator via the WSM phase by changing an external parameter m. If Fermi arcs connect creation pairs of Weyl nodes, w_1-w_2 and w_3-w_4, in Fig. 4(a), there will be (i) no surface state in the NI ($m < m_1$) and (ii) a single surface state in the TI phase ($m > m_2$) across the WSM → NI or WSM → TI transitions. It is consistent with that even (odd) number of surface states emerge and cross the Fermi level between time-reversal invariant momenta on the NI (TI) surface. On the other hand, if Fermi arcs connect annihilation pairs, w_1-w_3 and w_2-w_4 [shown in Fig. 4(b)], then another surface state appears in addition to the Fermi arcs resulting in the emergence of two (one) surface states in the NI (TI) phase. The GTT (STT) surface of the SET state of iPCM corresponds to the former (latter) case. A recent study of the band-bending effect [37]

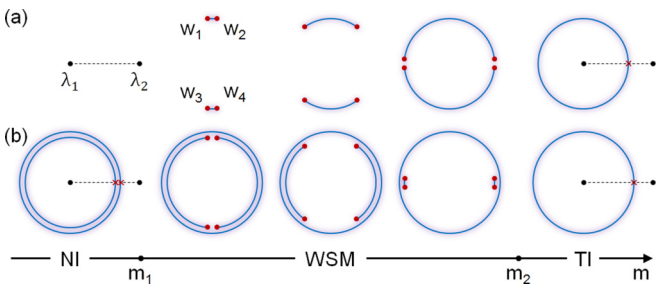

FIG. 4. Schematic view of Fermi arc connectivity. Two types of surface-state evolution as the system undergoes a topological phase transition from normal insulator (NI) to Weyl semimetal (WSM) to topological insulator (TI) phases by changing an external parameter m. (a) Fermi arc connecting creation pair. (b) Fermi arcs connecting annihilation pair. λ_i denotes time-reversal-invariant momenta on the surface BZ and w_i are the Weyl nodes.

also showed that an emergent closed loop on the surface is accompanied by a partner exchange of Fermi arcs.

The appearance of the closed loop at the STT surface may hinder the observation of Fermi arcs in angle-resolved photoemission spectroscopy measurements because of its close proximity in momentum space. However, even with limited resolution, the spectral intensity on the $\bar{\Gamma}$-$\bar{M}$ lines should be twice of that on the $\bar{\Gamma}$-$\bar{K}$ lines. It is also worthwhile to note that the distance of about 0.1 Å^{-1} of the Fermi arcs from $\bar{\Gamma}$ is larger than that of other predicted hexagonal WSMs [38].

In conclusion, we predict that the highly conductive SET state is a *Weyl semimetal phase* due to the ferroelectric polarization of the GeTe block in contrast to the *topological insulating phase* of the low conductive RESET state. The emergent twelve Weyl nodes in the SET state cause a giant enhancement in the conductivity by a factor of 5–100 in comparison to the RESET state. This is an important memory device in which the conductivity contrast between the SET and the RESET states is attributed to the emergent Weyl nodes. Our results, implying a robust Weyl phase in the SET state, open a way to functionalize the iPCM and design novel devices. We also predict two types of Fermi arc connectivity in the SET state depending on the surface termination.

At the final stage of this study, we became aware of a related work [39] predicting the Weyl semimetal phase in the Ferro-GeTe PCM structure, which is consistent with our result.

The work at CSUN is supported by NSF-Partnership in Research and Education in Materials (PREM) Grant DMR-1205734 and by the US Army of Defense (DOD), Grant Contract number W911NF-16-1-0487. Y.-S. S. and S.-H. J. were supported by the National Research Foundation of Korea through SRC program (Contract No. 2011-0030046). J. Kim and R. Wu were supported by DOE-BES (Grants Nos. DE-FG02-05ER46237 and SC0012670). Calculations were performed on parallel computers at NERSC supercomputer centers.

[1] S. R. Ovshinsky, Reversible Electrical Switching Phenomena in Disordered Structures, Phys. Rev. Lett. **21**, 1450 (1968).

[2] W. Welnic, A. Pamungkas, R. Detemple, C. Steimer, S. Blügel, and M. Wuttig, Unravelling the interplay of local structure and physical properties in phase-change materials, Nat. Mater. **5**, 56 (2006).

[3] M. Wuttig and N. Yamada, Phase-change materials for rewriteable data storage, Nat. Mater. **6**, 824 (2007).

[4] J. Kim, J. Kim, and S.-H. Jhi, Prediction of topological insulating behavior in crystalline Ge-Sb-Te, Phys. Rev. B **82**, 201312 (2010).

[5] J. Kim, J. Kim, K.-S. Kim, and S.-H. Jhi, Topological Phase Transition in the Interaction of Surface Dirac Fermions in Heterostructures, Phys. Rev. Lett. **109**, 146601 (2012).

[6] R. E. Simpson, P. Fons, A. V. Kolobov, T. Fukaya, M. Krbal, T. Yagi, and J. Tominaga, Interfacial phase-change memory, Nat. Nanotechnol. **6**, 501 (2011).

[7] J. Tominaga, A. V. Kolobov, P. J. Fons, X. Wang, Y. Saito, T. Nakano, M. Hase, S. Murakami, J. Herfort and Y. Takagaki, Giant multiferroic effects in topological GeTe-Sb_2Te_3 superlattices, Sci. Technol. Adv. Mater. **16**, 014402 (2015).

[8] X. Yu and J. Robertson, Modeling of switching mechanism in GeSbTe chalcogenide superlattices, Sci. Rep. **5**, 12612 (2015).

[9] D. Bang, H. Awano, J. Tominaga, A. V. Kolobov, P. Fons, Y. Saito, K. Makino, T. Nakano, M. Hase, Y. Takagaki, A. Giussani, R. Calarco, and S. Murakami, Mirror-symmetric magneto-optical Kerr rotation using visible light in $[(GeTe)_2(Sb_2Te_3)_1]n$ topological superlattices, Sci. Rep. **4**, 5727 (2014).

[10] Z. Wang, Y. Sun, X.-Q. Chen, C. Franchini, G. Xu, H. Weng, X. Dai, and Z. Fang, Dirac semimetal and topological phase transitions in A_3Bi (A = Na, K, Rb), Phys. Rev. B **85**, 195320 (2012).

[11] Z. Wang, H. Weng, Q. Wu, X. Dai, and Z. Fang, Three-dimensional Dirac semimetal and quantum transport in Cd_3As_2, Phys. Rev. B **88**, 125427 (2013).

[12] Z. K. Liu, J. Jiang, B. Zhou, Z. J. Wang, Y. Zhang, H. M. Weng, D. Prabhakaran, S-K. Mo, H. Peng, P. Dudin, T. Kim, M. Hoesch, Z. Fang, X. Dai, Z. X. Shen, D. L. Feng, Z. Hussain, and Y. L. Chen, A stable three-dimensional topological Dirac semimetal Cd_3As_2, Nat. Mater. **13**, 677 (2014).

[13] H. Weyl, Elektron und Gravitation. I, Z. Phys. **56**, 330 (1929).

[14] H. Nielsen and M. Ninomiya, The Adler-Bell-Jackiw anomaly and Weyl fermions in a crystal, Phys. Lett. B **130B**, 389 (1983).

[15] A. A. Burkov, M. D. Hook, and Leon Balents, Topological nodal semimetals, Phys. Rev. B **84**, 235126 (2011).

[16] K.-Y. Yang, Y.-M. Lu, and Y. Ran, Quantum Hall effects in a Weyl semimetal: Possible application in pyrochlore iridates, Phys. Rev. B **84**, 075129 (2011).

[17] X. Wan, A. M. Turner, A. Vishwanath, and S. Y. Savrasov, Topological semimetal and Fermi-arc surface states in the electronic structure of pyrochlore iridates, Phys. Rev. B **83**, 205101 (2011).

[18] H. Zhang, C.-X. Liu, X.-L. Qi, X. Dai, Z. Fang, S.-C. Zhang, Topological insulators in Bi_2Se_3, Bi_2Te_3 and Sb_2Te_3 with a single Dirac cone on the surface, Nat. Phys. **5**, 438 (2009).

[19] C. Pauly, G. Bihlmayer, M. Liebmann, M. Grob, A. Georgi, D. Subramaniam, M. R. Scholz, J. Sánchez-Barriga, A. Varykhalov, S. Blügel, O. Rader, and M. Morgenstern, Probing two topological surface bands of Sb_2Te_3 by spin-polarized photoemission spectroscopy, Phys. Rev. B **86**, 235106 (2012).

[20] B. Sa, J. Zhou, Z. Sun, J. Tominaga, and R. Ahuja, Topological Insulating in $GeTe/Sb_2Te_3$ Phase-Change Superlattice, Phys. Rev. Lett. **109**, 096802 (2012).

[21] C. Pauly, M. Liebmann, A. Giussani, J. Kellner, S. Just, J. Sánchez-Barriga, E. Rienks, O. Rader, R. Calarco, G. Bihlmayer, and M. Morgenstern, Evidence for topological band inversion of the phase change material, Appl. Phys. Lett. **103**, 243109 (2013).

[22] D. D. Sante, P. Barone, R. Bertacco, and S. Picozzi, Electric control of the giant Rashba effect in bulk GeTe, Adv. Mater. **25**, 509 (2013).

[23] M. Liebman, C. Rinaldi, D. Di Sante, J. Kellner, C. Pauly, R. N. Wang, J. E. Boschker, A. Giussani, S. Bertoli, M.

Cantoni, L. Baldrati, M. Asa, I. Vobornik, G. Panaccione, D. Marchenko, J. Sánchez-Barriga, O. Rader, R. Calarco, S. Picozzi, R. Bertacco, and M. Morgenstern, Giant Rashba-type spin splitting in ferroelectric GeTe(111), Adv. Mater. **28**, 560 (2016).

[24] S. Murakami, Phase transition between the quantum spin Hall and insulator phases in 3D: Emergence of a topological gapless phase, New J. Phys. **9**, 356 (2007).

[25] S. Murakami and S.-I. Kuga, Universal phase diagrams for the quantum spin Hall systems, Phys. Rev. B **78**, 165313 (2008).

[26] A. A. Burkov and Leon Balents, Weyl Semimetal in a Topological Insulator Multilayer, Phys. Rev. Lett. **107**, 127205 (2011).

[27] G. Kresse and J. Furthmüller, Efficient iterative schemes for *ab initio* total-energy calculations using a plane-wave basis set, Phys. Rev. B **54**, 11169 (1996).

[28] G. Kresse and J. Furthmüller, Efficiency of *ab-initio* total energy calculations for metals and semiconductors using a plane-wave basis set, Comput. Mater. Sci. **6**, 15 (1996).

[29] P. E. Blöchl, Projector augmented-wave method, Phys. Rev. B **50**, 17953 (1994).

[30] G. Kresse and D. Joubert, From ultrasoft pseudopotentials to the projector augmented-wave method, Phys. Rev. B **59**, 1758 (1999).

[31] J. P. Perdew, K. Burke, and M. Ernzerhof, Generalized Gradient Approximation Made Simple, Phys. Rev. Lett. **77**, 3865 (1996).

[32] S. Grimme, Semiempirical GGA-type density functional constructed with a long-range dispersion correction, J. Comp. Chem. **27**, 1787 (2006).

[33] A. A. Mostofi, J. R. Yates, G. Pizzi, Y.-S. Lee, I. Souza, D. Vanderbilt, and N. Marzari, An updated version of WANNIER90: A tool for obtaining maximally-localised Wannier functions, Comput. Phys. Commun. **185**, 2309 (2014).

[34] F. Tran and P. Blaha, Accurate Band Gaps of Semiconductors and Insulators with a Semilocal Exchange-Correlation Potential, Phys. Rev. Lett. **102**, 226401 (2009).

[35] D. Koller, F. Tran, and P. Blaha, Improving the modified Becke-Johnson exchange potential, Phys. Rev. B **85**, 155109 (2012).

[36] I. A. Nechaev, I. Aguilera, V. De Renzi, A. di Bona, A. Lodi Rizzini, A. M. Mio, G. Nicotra, A. Politano, S. Scalese, Z. S. Aliev, M. B. Babanly, C. Friedrich, S. Blügel, and E. V. Chulkov, Quasiparticle spectrum and plasmonic excitations in the topological insulator Sb_2Te_3, Phys. Rev. B **91**, 245123 (2015).

[37] I. P. Rusinov, T. V. Menshchikova, I. Yu. Sklyadneva, R. Heid, K.-P. Bohnen, and E. V. Chulkov, Pressure effects on crystal and electronic structure of bismuth tellurohalides, New J. Phys. **18**, 113003 (2016).

[38] J. Liu and D. Vanderbilt, Weyl semimetals from noncentrosymmetric topological insulators, Phys. Rev. B **90**, 155316 (2014).

[39] S. V. Eremeev, I. P. Rusinov, P. M. Echenique, and E. V. Chulkov, Temperature-driven topological quantum phase transitions in a phase-change material $Ge_2Sb_2Te_5$, Sci. Rep. **6**, 38799 (2016).